Aerosol immission maps and trends over Germany with hourly data at four rural background stations from 2009 to 2018

Jost Heintzenberg[1], Wolfram Birmili[2], Bryan Hellack[2], Gerald Spindler[1], Thomas Tuch[1], and Alfred Wiedensohler[1]

1: Leibniz Institute for Tropospheric Research (TROPOS), Permoserstr. 15, 04318 Leipzig, Germany

2: German Environment Agency, Wörlitzer Platz 1, 06844 Dessau-Roßlau, Germany

Abstract

Ten years of hourly aerosol and gas data at four rural German stations have been combined with hourly back trajectories to the stations and inventories of the European EDGAR emission database yielding immission maps over Germany of PM_{10}, particle number concentrations, and equivalent black carbon (eBC). The maps reflect aerosol emissions modified with atmospheric processes during transport between sources and receptor sites. Compared to emission maps strong Western European emission centers do not dominate the downwind concentrations because their emissions are reduced by atmospheric processes on the way to the receptor area. PM_{10}, eBC, and to some extent also particle number concentrations are rather controlled by emissions from Southeastern Europe from which pollution transport often occurs under dryer conditions. Newly formed particles are found in air masses from a broad sector reaching from Southern Germany to Western Europe which we explain with gaseous particle precursors coming with little wet scavenging from this region.

Annual emissions for 2009 of PM_{10}, BC, SO_2, and NO_x were accumulated along each trajectory and compared with the corresponding measured time series. The agreement of each pair of time series was optimized by varying monthly factors and annual factors on the 2009

emissions. This approach yielded broader summer emission minima than published values that were partly displaced from the midsummer positions. The validity of connecting immission and emission of particulate pollution was tested by calculating temporal changes of eBC for subsets of back trajectories passing over two separate prominent emission regions, region A to the Northwest and B to the Southeast of the measuring stations. Consistent with reported emission data the calculated immission decreases over region A are significantly stronger than over region B.

1 Introduction

The atmospheric aerosol is known to influence the Earth's radiation budget because it directly scatters and absorbs solar radiation (Schwartz, 1996; Bond et al., 2013), and acts as cloud condensation nuclei, thus modulating the optical properties and lifetimes of clouds (Twomey, 1974; Penner et al., 2004). In many regions of the globe that had undergone industrialization early on, anthropogenic aerosol concentrations are currently in decline (Leibensperger et al., 2012; Zanatta et al., 2016). With respect to declining concentrations and emissions, Samset al. (2018) suggest that removing present-day anthropogenic aerosol emissions – assuming constant greenhouse gas emissions, could lead to a global mean surface heating as high as 0.5–1.1°C.

Besides climate, the atmospheric aerosol has been acknowledged to influence human health through respiratory and cardiovascular health endpoints (Anderson et al., 2012). Lelieveld et al., (2015) quantified the world-wide burden of disease (premature mortality) due to outdoor pollution, large part of which was attributed to airborne particulate matter. It is apparent that the distribution of adverse health effects is very uneven among the world-wide population, depending on the local level of outdoor pollution.

In view of the described man-driven effects it seems imperative to develop instruments to reliably monitor changes in anthropogenic aerosol concentrations as well as an understanding of the balance between aerosol sources and measured concentrations. Researchers have strived to obtain a spatial picture of the distribution of pollutants, and to achieve a connection between the sources of pollution and concentrations downwind. A widely used method has been the extrapolation of concentrations measured in one or several locations into two-dimensional space through the use of meteorological dispersion approaches: The first maps of particulate

air pollutants over Europe were constructed in the 1970s with the help of coarse emission data and simple trajectory models (Eliassen, 1978). Statistical methods were developed to connect pollution sources and ensuing aerosol concentrations at receptor sites (Miller et al., 1972; Friedlander, 1973; Cass and McRae, 1983). By combining statistics with back trajectory data sectorial information about sources controlling the composition of the aerosol over Southern Sweden was derived by Swietlicki et al., (1988). Later the approach of using back trajectories to map aerosol sources was refined by Stohl (1996) and tested with one-year sulfate data from the co-operative program for monitoring and evaluation of the long-range transmission of air pollutants in Europe (EMEP, www.emep.int). In a similar approach with five years of aerosol data from a single Siberian receptor site Heintzenberg et al. (2013) identified potential source regions over Eurasia and with aerosol data from four Swedish icebreaker expeditions over the Central Arctic (Heintzenberg et al., 2015). Charron et al. (2008) constructed concentration field maps to identify the source regions of specific types of aerosol particle size distributions arriving in England. All these works share the approach that time-dependent information on concentrations measured at receptor site(s) are transformed into space, thus allowing conclusions on the potential source regions of gaseous and/or particulate emissions.

With more comprehensive air quality models concentrations of specific aerosol were mapped over Europe together with short temporal developments (e.g., Schell et al., 2001). For specific episodes high spatial resolution aerosol concentration maps in urban and non-urban European areas have been generated with sophisticated chemistry transport models (e.g., Beekmann et al., 2015; Riemer et al., 2004; Wolke et al., 2004). For the years 2002 and 2003 Marmer and Langman (2007) analyzed the spatial and temporal variability of the aerosol distribution over Europe with a regional atmosphere-chemistry model. They found that meteorological conditions play a major role in spatial and temporal variability in the European aerosol burden distribution. Regionally, year to year variability of modeled monthly mean

aerosol burden reached up to 100% because of different weather conditions.

In the present study ten years of hourly aerosol data at four German stations were available for the identification of potential source regions. As it appears unrealistic to analyze such a large database with advanced chemical transport models we resorted to the well proven approach of utilizing back trajectories cited above and connected the results to emission fields. We define the resulting concentration maps of particulate and gas parameters as immission maps because they represent long-term average emissions of air pollutants modified by the controlling atmospheric processes along the pathways to the receptor sites. In Charron et al. (2008) this approach is termed "concentration field map method". With a much larger data set spanning a much tighter network of 1500 stations Rohde and Muller (2015) used the Kriging interpolation approach (Krige, 1951) to construct air pollution maps over China. Another approach to construct pollution maps over the province Henan, China was used by Liu et al., (2018). They combined an emission inventory with chemical modeling and back trajectories to derive high resolution maps of particulate and gaseous pollution components and find that emissions from neighboring provinces are important contributors to local air pollution levels.

Recent political, economic and technological developments in Europe have caused substantial changes in the emission of air pollutants. Lavanchy et al. (1999) deduced a trend in atmospheric black carbon from preindustrial times to 1975. Strong downward trends in major aerosol components before and after the German reunification (1983-1998) over rural East Germany were reported by Spindler et al., (1999). For the years 2003 – 2009 Kuenen et al., (2014) published trends in the development of aerosol emissions as elaborated from reported emissions. The German Environmental Agency (GEA) publishes trends in air pollution as measured at a number of ca. 380 federal and state air quality stations (Minkos, 2019).

According to these records, PM_{10} mass concentrations declined by approximately 25 % over the period 2000-2019

Combining long-term aerosol and gas data at the four stations of the present study provide an excellent data base for identifying both the most important source regions and possible temporal changes. During the ten recent years covered by our data we expected noticeable systematic changes in our time series that can be interpreted in terms of emissions. As a side result in the process of deriving long-term emission trends of major air pollutants over Germany information of the monthly disaggregation of annual aerosol emissions can be derived.

2 Aerosol and trace gas data

The core data of the present study have been measured at the stations Melpitz (ME), Neuglobsow (NG), and Waldhof (WA) of the German Ultrafine Aerosol Network GUAN network (Birmili et al., 2016) and at station Collmberg (CO) operated by the Saxonian Environment Agency. These four rural background stations lie in the northeastern lowlands of Germany at distances between 30 and 205 km from each other. Ten-year-average particle mass concentrations under 10 µm particle diameter (PM_{10}) and their standard deviations at the four stations are rather similar: 15±13, 22±12, 14±10, and 15±11 μgm^{-3} at CO, ME, NG, and WA, respectively. The corresponding long-term average particle number concentrations between 10 and 800 nm particle diameter ($N_{10\text{-}800}$) and their standard deviations at the three GUAN-stations are 5400±4100, 3600±2300, and 4300±2800 cm^{-3}, respectively. Basic statistics on particle number and eBC mass concentrations of the three GUAN-stations were presented in Sun et al. (2019) whereas details about instrumentation and their maintenance can be found in Birmili et

al., (2016). The ensemble of hourly data at the four stations is the base of the pollution maps derived in this work.

TROPOS-type mobility particle size spectrometers (MPSS, Wiedensohler et al., 2012) were used to record particle number size distributions across the particle size range 10-800 nm. Quality assurance of the long-term measurements followed the recommendations of Wiedensohler et al. (2018) including weekly inspections as well as monthly and annual maintenance intervals. Once a year the MPSS were intercompared against a reference MPSS of the WCCAP (World Calibration Center for Aerosol Physics) either on-site and/or at the calibration facility. The lower detection limit of the MPSS is around 30 cm^{-3} for a time resolution of 30 minutes. Equivalent Black Carbon (eBC) was determined by multi-angle absorption photometers (MAAP) using a mass absorption cross section of 6.6 $m^2\ g^{-1}$ (Petzold et al., 2013; Nordmann et al., 2013; Birmili et al., 2016). An intercomparison of multiple MAAP instruments resulted in an inter-device variability of less than 5% (Müller et al., 2011). While the MAAP deployed at the TROPOS station Melpitz was biannually compared to the reference absorption photometer at the WCCAP in Leipzig, the instruments at the UBA stations Waldhof and Neuglobsow were serviced by the manufacturer. For hourly measurements of PM_{10} continuous oscillating microbalances (Thermo Scientific TEOM 1400) were utilized at stations CO, NG, and WA. At station ME PM_{10} was determined in daily filter samples (0:00 to 24:00 CET), Spindler et al. (2013). The TEOM1400-instrument and gravimetric filter sampling are different methods for particle mass concentrations. The TEOM collects particulate mass on a vibrating substrate (tapered element) and registers the change of the oscillation frequency that is decreasing with mass loading (Patashnick and Rupprecht, 1991). The TEOM operates at a constant temperature setting above ambient (typically 30– 50°C) to prevent contraction and expansion of the tapered element and reduce interferences from water vapor condensation. However, heating the ambient air enhances volatilization of particle-

bound semivolatile compounds (e.g., ammonium nitrate and some organic species) resulting in an underestimation of PM when semivolatile material dominates the particulate phase during cold seasons. The condensation and evaporation of ammonium nitrate and organic species can also influence the filter sampling under ambient conditions. Here the effect can be balanced partly by the temperature variation during the daily filter sampling. However, the results of both methods mostly are in good agreement (e.g., Zhu et al., 2007).

Hourly aerosol data from the three GUAN-stations during 2009 – 2015 (NG ≥2011) have been utilized in a previous study (Heintzenberg et al., 2018) to understand aerosol processes during air mass transport between the stations. In the present study the data set was enlarged to include the additional station Collmberg and data at all stations from the year 2016 through 2018. The integral aerosol parameters particle number concentration ($N_{10\text{-}800}$, cm^{-3}), light absorption-equivalent mass concentration of Black Carbon (eBC, μgm^{-3}), and particle mass concentrations under 10 µm particle diameter (PM_{10}, μgm^{-3}) were utilized. $N_{10\text{-}800}$ is based on the integral over measured particle size distributions from 10 to 800 nm.

NO_x and SO_2 emitted by anthropogenic combustion processes are transformed in the atmosphere and add to the anthropogenic aerosol. At the three GUAN stations both are measured with the same temporal resolutions as the aerosol data. Additionally, at Collmberg NO_x-data could be utilized in the interpretation of the aerosol data. The trace gas analyzers for NO_x and SO_2 were calibrated with test gases for NO (NO in N_2) and SO_2 (SO_2 in N_2, both Air Liquide, Germany). NO_2 was produced in a gas phase titration device (GPT APMC370, Horiba, Germany) by quantitative oxidation of NO test gas (Rehme, 1976). The trace gas analyzers were used in an optimal range and all registered values (also below the detection limit) were used for this long-term study. As most particle numbers in polluted continental environments tropospheric ozone is a secondary atmospheric pollutant. We utilized hourly

ozone data taken at all four stations throughout the studied time period as ancillary information in the discussion of particle-number related results. For the ozone measurements a common trace gas ozone monitor was used (Horiba APOA-350). This device quantifies tropospheric ozone by UV Absorption and use the cross-flow modulation principle. Ambient air with and without ozone (elimination by a selective scrubber) was used alternatively in the measuring cuvette yielding a very stable ozone signal. The devices were calibrated using an ozone-standard (Ozon-Calibrator, Thermo Environmental Instruments 49PS).

Table 1 gives an overview over the instrumental characteristics of all stations and the total number of validated data hours for each utilized component. The minimum is 57962 hours for validated MPSS-data at the three GUAN-stations and the maximum with 88838 validated data hours for NO_x at all four stations. Strictly concurrent (by the hour) are less validated data hours. For MPSS, eBC, and SO_2-data at the GUAN-stations this numbers is 48533 hours, and 48114 and 47729 hours for PM_{10} and NO_x-data, respectively, at all four stations. However, these reduced strictly concurrent numbers do not substantially affect the 10-year-average maps discussed below.

3 Back trajectories

With the HYSPLIT4 model (Stein et al., 2015) and based on the meteorological fields from the Global Data Assimilation System with one-degree resolution (GDAS1, https://www.emc.ncep.noaa.gov/gmb/gdas/) three-dimensional trajectories were calculated arriving every hour at a height of 500m above ground level at the four stations. The trajectories were calculated backward for up to five days using the meteorological fields from the server at

214 Air Resources Laboratory (ARL), NOAA (http://ready.arl.noaa.gov), where more information
215 about the GDAS dataset can be found. In the immission maps constructed with extrapolated
216 measurements at the stations and in any comparisons with emissions along the back trajectories
217 only trajectory points under 1000 m altitude above ground were utilized. Turbulent
218 atmospheric mixing is included in parameterized form in HYSPLIT4. The present study
219 utilizes the default version of this parameterization according to Draxler and Hess (1998). The
220 back trajectories are calculated with the base version of HYSPLIT4 that does not include any
221 specific dispersion and scavenging of atmospheric trace substances. Precipitation along the
222 trajectories was used in the interpretation of the immission maps. The precipitation values
223 mapped in the present study and the temperature values used in the trend discussion of $N_{10\text{-}800}$
224 are those listed by HYSPLIT4 at each point of a trajectory. They are meteorological parameters
225 at the nearest grid cell of the assimilated global meteorological fields provided by the U.S.
226 National Weather Service's National Centers for Environmental Prediction (NCEP)
227 (Kanamitsu, 1989). Average horizontal wind speeds in between two one-hour trajectory steps
228 were calculated from the distance covered by a trajectory between two successive steps. With
229 the 350593 hourly back trajectories from the four stations the time series of $N_{10\text{-}800}$, PM_{10}, and
230 eBC were extrapolated over Germany and part of the neighbor countries. At Melpitz PM_{10}-
231 data were only available as daily averages. Thus, the daily average concentrations were
232 extrapolated along each hourly trajectory of the respective day.
233
234
235 ## 4 Emission data
236
237 For the interpretation of the immission maps we used the emission data set version 4.3.2 for
238 2009 of the components particle mass concentrations below 10 μm (PM_{10}), BC, NO_x and SO_2

as compiled in the Emissions Data Base for Global Atmospheric Research (EDGAR, https://edgar.jrc.ec.europa.eu/overview.php?v=432_AP, DOI (https://data.europa.eu/doi/10.2904/JRC_DATASET_EDGAR). This data set concerns primary emissions only and has been introduced by Crippa et al., (2018). All human activities, except large scale biomass burning and land use, land-use change, and forestry are included in the data base. Emissions of coarse particles from agricultural surfaces are not included. They are, in fact, very sensitive to soil and weather conditions, and thus not trivial to quantify. Primary aerosol emission data are generally characterized by rather high uncertainties. For the EDGAR data base Crippa et al. (2018) report a range of variation in 2012 between 57.4% and 109.1% for PM_{10}, and between 46.8% and 92% for BC. Even higher uncertainties in PM emissions might come from super-emitting vehicles that are not considered in this data base (Klimont et al., 2017). In our maps and trend calculations we applied the grid values of emission data that were listed in the EDGAR inventories no more than 30 km away from any trajectory time step.

5 Results and discussion

5.1 Aerosol concentration maps (immission maps

The trajectory-extrapolated $N_{10\text{-}800}$, PM_{10}, and eBC from the four stations yielded immission maps averaged over the period 2009 – 2018, that are collected in Figs. 1-2. Both, the particle-number related $N_{10\text{-}800}$ and the particle-mass related PM_{10}, and eBC exhibit systematic seasonal variations. Most events of new particle formation (NPF) over the continents occur during the photochemically active summer months (Kulmala et al., 2004) whereas the particle-mass related aerosol parameters due to combustion processes exhibit highest concentrations during the winter months (Matthias et al., 2018). Consequently, we constructed two maps for each discussed component: One of averages over the months April through October and one of

averages over the months November through March. Only map cells with at least 300 trajectory hits are discussed. Interpreting these hits in terms of Poisson-statistics would then yield a maximum uncertainty of 5.8% per cell. In terms of a Gaussian statistic the arithmetic cell-averages displayed in the maps exhibit standard deviations of cell averages that are less than six percent.

The maps of $N_{10\text{-}800}$ in Fig. 1 show distributions of air masses over Germany and adjacent countries related to particle numbers instead of particulate mass. There are two arguments for showing maps of number related results. First, particle number concentrations are connected with cloud processes, their formation (Pruppacher and Klett, 1978), radiative effects, e.g., albedo (Twomey, 1974), and precipitation (Li et al., 2011). Second, in the area of aerosol-health issues ultrafine particles (< 100 nm diameter) have been gaining attention in recent years (Wichmann and Peters, 2000), i.e. an increasing number of health effects is attributed rather to particle number than to particle mass. The fact that NPF-events occur concurrently in or near the top of the continental planetary boundary layer over wide geographical regions (e.g., Wehner et al., 2007) is partly due to concurrent advantageous photochemical conditions allowing for the formation of condensable vapors, in particular global radiation (Birmili et al., 2001). Two other factors constraining NPF are the availability of gaseous particle-precursors and the concurrent pre-existing aerosol.

The summer map (4-10) of $N_{10\text{-}800}$ exhibits the high values in the Southwest-to-Northeast-sector of the map. Highest values are concentrated in a belt reaching from Burgundy through Switzerland, Southern Germany, Czech Republic to Southwestern Poland. Interestingly, this belt of high $N_{10\text{-}800}$ is collocated to large extent with a belt of high summer ozone concentrations (cf. Fig. S1). This photochemically controlled pollutant (Monks et al., 2015) exhibits highest summer concentrations in air masses from Southwestern Poland and Northern Czech Republic,

290 a region from which high ozone values are reported (Struzewska and Jefimow, 2013; Hůnová,
291 2003; Hůnová and Bäumelt, 2018). However, the summer map of $N_{10\text{-}800}$ does not show the
292 highest values in air masses from the region with highest ozone pollution. High particle
293 numbers in air masses coming over the Alps from Northern Italy may be related to the high
294 emissions of air pollutants in the Po Valley that are known to reach frequently through so called
295 alpine pumping (Winkler et al., 2006; Lugauer and Winkler, 2005; Reitebuch et al., 2003) over
296 the mountains. The high NO_x-concentrations in air masses from Northern Italy in both summer
297 and winter maps (see Fig. S2) indicate that pollution from south of the Alps can even reach
298 Northeastern Germany. In the winter map of $N_{10\text{-}800}$ (11-3 in Fig. 1) the belt of highest summer
299 values is apparently complemented by more transalpine pollution transport and by transport
300 from the Southeast. The lower photochemical activity in winter is reflected in the lower winter
301 ozone concentrations in Fig. S1, albeit transalpine pollution transport is still visible in the winter
302 map of NO_x in Fig. S2. Northwestern Italy also shows up as an emission hot spot in the maps
303 of trajectory-summed emissions in Fig. S4.
304
305 In both summer and winter the maps of PM_{10}, and eBC in Fig. 2 exhibit a clear Northwest-
306 to-Southeast structure with the cleanest sector being in the Northwest covering the coastal area
307 of the North Sea, the BENELUX countries Belgium, the Netherlands, and Luxemburg, and
308 Northwestern Germany. The strongest contrast between the cleanest Northwesterly and the
309 most polluted Southeasterly map sectors is seen in the winter map of eBC. Highest average
310 concentrations are measured in airmasses from the Southeastern half of the map, most strongly
311 expressed in PM_{10} and eBC with maxima in a region leading from Southwest Poland through
312 the Czech Republic, Slovakia, Austria, and former Yugoslavia to Northeastern Italy. The back
313 trajectories in the Southeastern sector of the maps for PM_{10} and eBC point towards countries,
314 in which the emissions of air pollution in the past 20 years developed very differently as
315 compared to those in Western Europe. According to the European Environment Agency

316 (https://www.eea.europa.eu/data-and-maps/dashboards/air-pollutant-emissions-data-viewer-2)
317 the latter parts of Western Europe experienced a strong and nearly monotonous decrease in
318 emissions of PM_{10} whereas the emissions in Poland, Czech Republic, Slovakia, Austria, former
319 Yugoslavia, and Italy stayed nearly constant or even increased in recent years after the dramatic
320 decreases in the course of the political developments of the 1990ies. The seasonal maps of the
321 combustion derived SO_2 in Fig. S3 look very similar to the those of the particle-mass related
322 maps of PM_{10} and eBC, again the strongest NW/SE-contrast visible in winter.
323
324 5.2. Pollutant emissions and atmospheric processes
325
326 In Fig. 3 annual average emissions of PM_{10}, BC, SO_2, and NO_x are mapped for 2009 according
327 to the EDGAR emission database. Except for the absolute numbers the maps for SO_2, and NO_x
328 look rather similar to those for particulate emissions. They all emphasize highly populated and
329 industrialized emissions center. Beyond that the SO_2-map accentuates individual large
330 combustion sources such as conventional power plants. Whereas the strong emissions in
331 Northern Italy are seen in the maps of PM_{10}, BC, and NO_x emissions in the countries in the
332 Southeastern sector of the maps by no means reflect the high concentrations of particulate
333 components seen in the immission maps of Figs. 1 and 2.
334
335 The seeming discrepancy between the immission maps in Figs. 1 and 2 and the emission
336 maps of Fig. 3 can be resolved. For that purpose, the EDGAR-emissions of PM_{10}, BC, SO_2,
337 and NO_x along all 350593 hourly back trajectories to the four stations during the ten studied
338 years were summed up. Then the sums were extrapolated back along each trajectory. In Fig.
339 S4 10-year average maps of these extrapolated emission sums are displayed. As in Fig. 3 except
340 for the absolute numbers there is a strong similarity between the four mapped component sums.
341 Because of the integral nature of the mapped results one cannot expect the maps in Fig. S4 to

342 locate correctly specific emission centers. However, they certainly indicate the map sectors
343 from which the most substantial emissions could have reached the stations. As in Figs. 1 and
344 2 the Southeastern sectors of the maps of integrated emissions most prominently show up.
345 Interestingly, the maps in Fig. S4 also indicate the highly polluted region of Northwestern Italy
346 (Diémoz et al., 2019a; Diémoz et al., 2019b). The emissions from the emission centers in
347 Northwestern Europe are hardly discernible in Fig. S4. They do show up (most strongly in Fig.
348 S4c for SO_2-emission sums) as apparent emissions over the adjacent North Sea. We interpret
349 the "misplaced" emissions over the North Sea as air mass transport from the North Sea via the
350 emission region in the BENELUX countries to the receptor sites that was not compensated by
351 other low pollution air transport from the North Sea to the stations that had not passed over the
352 Northwestern European emission centers.
353
354 Two major atmospheric processes will reduce the concentrations of emitted or in situ formed
355 aerosol particles: dilution through mixing with cleaner air masses and wet scavenging through
356 in-cloud and sub-cloud processes. As a tracer of the first of these two processes Fig. 4a gives
357 the long-term average geographical distribution of trajectory derived wind speed over the study
358 area. Highest average wind speeds and ensuing atmospheric mixing is seen over the major
359 emission centers of Northwestern Germany, the BENELUX countries and adjacent seas
360 whereas lowest wind speeds are seen over Northern Germany and the Southeastern neighbor
361 countries. The long-term average geographical distribution of precipitation as taken by
362 HYSPLIT from the GDAS meteorological fields in Fig. 4b corroborates the results about
363 atmospheric cleaning processes indicated in Fig. 4a. The small absolute numbers in Fig. 4b are
364 due to the episodic nature of precipitation: most of the time it does not rain or snow. The blue
365 crescent reaching from the North Sea through the BENELUX countries, Eastern France,
366 Switzerland and the alpine region exhibits maximum precipitation values while Southern and
367 Eastern Germany with the adjoining countries to the East and Southeast show minimum

368 precipitation values. Thus, in the long term we expect much of the high Western European
369 emissions to be scavenged to a substantially by wet processes. In addition, air masses arriving
370 from Western and Northwestern directions at the stations usually cross the Western European
371 emission centers with much lower pollution burdens than air masses coming from the polluted
372 countries of Southeastern Europe arriving at the corresponding map borders (cf. Fig. PM_{10} —
373 36th maximum daily average value in μg m^{-3}, 2005 in EEA, 2009).
374
375 **5.3. Immission trends for air from specific source regions**
376
377 As mentioned in the introduction, the pollutant emissions reported by the European and national
378 Environment Agencies represent a synthesis of known pollutant sources combined with
379 assumed emission factors. These emissions are typically used as input for air quality modelling
380 and subsequent assessment, as well as for trend analyses. However, it remains unclear to what
381 extent these reported emissions are realistic, and whether their trends represent the trend in true
382 emissions. Here, we attempt to assess spatially-resolved trends in real particulate emissions by
383 an analysis of measured concentrations (immissions) in air masses travelling over source-
384 specific regions.
385
386 To test our method, we selected two pronounced source regions in Europe, located within
387 1000 km distance from our observation sites. These regions were defined by emission hotspot
388 regions that can be seen in the EDGAR emission maps in Fig. 3a-b and comprise: Region A
389 (Be-NL-NRW; comprising most of Belgium, southern parts of the Netherlands, and much of
390 the German state North Rhine-Westphalia) and Region B (CZ-PL-SK; comprising the central
391 parts of the Czech Republic, southern parts of Poland, and adjacent areas of Slovakia.)
392 According to the European Environment Agency (EEA) these are regions, where reported

particulate emissions have developed differently during the past 10 years. Our goal is to verify this through an analysis of real atmospheric observations over this period.

Temporal trends were computed using the customized Sen–Theil trend estimator (Sen, 1968; Theil, 1992). The Sen–Theil estimator is the median of many slopes calculated in a continuous or non-continuous time series, with its robustness against outliers being one of its main assets. For the detailed description of this trend estimator we refer to Sun et al. (2020), Section 2.3.1. Here we computed the Sen–Theil estimator for hourly observation data at stations ME, NG, and WA. Subsets of back trajectories were selected that spent at least 1, 3 , 6, or 12 hours over the source regions A and B. Depending on that criterion, different sub-sets were analyzed. The difference in median eBC mass concentration between air masses arriving from source region A and B is obvious, as could already be determined in the corresponding immission maps (Fig. 2c-d). As we learned from Sect. 5.2 these immission maps are strongly influenced by the different meteorological conditions governing atmospheric dispersion in different wind direction, so that these values allow no direct conclusion on the strength of emission sources located upwind.

We analyzed the temporal trends in eBC over the period 2009-2018 for the subsets belonging to Regions A and B – assuming that these systematic differences in meteorological conditions should even out over such long observation periods. Table 2 shows that the Sen–Theil slope estimator for Region A is between -7.6 % and -5.1 % for the three observation sites and the requirement of a back trajectory to have spent at least 6 hours over Region A. For region B, the corresponding Sen–Theil slope estimators are between -4.0 % and -2.7 % for the observation sites. As we can read from these results, the annual decrease in eBC is more pronounced for air masses that have travelled over Region A.

Between 2009 and 2017 for the EU member states of Belgium, the Netherlands, Germany, the Czech Republic, Poland, and Slovakia the annual rates of decrease in reported emissions were between -4.9 and -6.1 % for the first three countries, and between +0.5 and -2.8% for the latter three (https://www.eea.europa.eu/data-and-maps/dashboards/air-pollutant-emissions-data-viewer-2). As compiled in Table 2 these reported trends are largely consistent with the rates of changed derived from our eBC immission trends. Although we need to keep in mind that the six nation states only partially contribute to our regions A and B, it seems valid to conclude that BC emissions in region A indeed decreased more rapidly in the past decade compared to region B. Our approach seems able to differentiate between concentrations trends in air masses that have passes over rather different source regions. This might represent a step towards the assessment of changes in real-world emissions allocated in specific source regions over multi-annual periods.

5.4. Comparison of immission and emission trends

Besides the map comparison a second approach was used to connect emission data with the measured aerosol time series. Along each of the hourly back trajectories the emissions according to the EDGAR database were summed up. Then monthly medians of the emission sums and the measured parameters were formed. The EDGAR database reports annual average emissions. PM_{10}, black carbon and other combustion related air pollutants show substantial annual variations with high winter and low summer values at non-urban sites (e.g., Heintzenberg and Bussemer, 2000). In emission modeling the temporal variation of annually reported emissions is considered by disaggregating the annual values with monthly, weekly and daily factors (Matthias et al., 2018). For the time-resolved comparison of PM_{10} and BC-emissions with PM_{10} and eBC-concentrations at the GUAN-sites monthly medians of PM_{10} and eBC-values at the stations were formed and plotted in Fig. 5. We expected both, seasonal

variations and a long-term trend in the emissions. For M hours per month of measured components at the four stations the annual average EDGAR-emissions E_{PM10}, E_{BC}, E_{SO2}, and E_{NOx} were summed up along the 121 trajectory steps leading to the stations. Then monthly medians $\tilde{E}_{i=1,4}$ were formed according to Eq. 1 (exemplified for BC). Medians were chosen to reduce the effect of outliers due to local emission and scavenging events.

$$\tilde{E}_{BC} = Median\left(\sum_{n=1}^{121} E_{BC}\right)_{m=1,M} \quad \text{Eq. 1}$$

The monthly median emission sums $\tilde{E}_{i=1,4}$ were modified with a monthly (f_m) and an annual factor (g_y) in order to simulate respective median monthly measured concentrations taken over all stations. Thus, for each component 12 monthly and 10 annual trend factors determined the agreement of modified summed emissions and measured concentrations. As objective or utility function χ^2 the sum of squared deviations between annually and monthly modified emission sums and monthly median measured concentrations was formed taken over the 120 months of the present study (exemplified for BC in Eq. 2).

$$\chi^2_{BC} = \sum_{j=1}^{120}\left(f_{m=1,12} \cdot g_{y=1,10} \cdot \tilde{E}_{BC} - eBC\right)^2 \quad \text{Eq. 2}$$

χ^2 was minimized with a Generalized Reduced Gradient (GRG) solver (Lasdon et al., 1978) that optimized the12 monthly and 10 annual factors for each of the four measured components. We used Excel's® implementation of the GRG-solver procedure for the optimization. After optimizing month and trend factors the average relative deviation between emission-simulated and measured monthly median curves is 14%, 21%, 25%, and 18% for PM_{10}, eBC, SO_2, and NO_x, and respectively. The optimized monthly median emission sums for all four parameters are displayed in Fig. 5 together with the measured monthly median concentrations.

469

470 A ten-year trend in emissions of PM_{10}, BC, SO_2, and NO_x, and average monthly factors for
471 the respective parameters are the two essential results derived from the optimization approach.
472 The ten-year trends relative to 2009 are collected in Fig. 6. Annual averages of the relative
473 differences between the monthly median measured parameters and the corresponding emission
474 derived parameters were formed and applied to the GUAN-trend values displayed in Fig. 6.
475 The resulting error bars on the trends serve as estimates of the uncertainties of the optimization
476 approach. The general trend in Fig. 6 is downward to minima between 30 and 70% of the 2009
477 values in 2016/17 after which all parameters exhibit increases, most strongly PM_{10}. SO_2 shows
478 the strongest decrease whereas PM_{10} and NO_x-emissions diminished the least. In 2010/2011
479 the trend curves of PM_{10} and NO_x in Fig. 6 show a slight increase that can be linked to a recovery
480 of economic activity after the world-wide financial and economic crisis during the period 2007-
481 2009. The increase in PM_{10} is also visible in the trend curves relative to
482 2005 published by the German Environment Agency
483 (https://www.umweltbundesamt.de/daten/luft/luftschadstoff-emissionen-in-
484 deutschland/emissionen-prioritaerer-luftschadstoffe).
485

486 The results of two comparisons of our trends with data reported by the German and European
487 Environment Agencies are added to Fig. 6. In general, the trends reported by the German
488 Environment Agency for all German emissions exhibit weaker reductions than the results of
489 the present study. Only for PM_{10} in 2011 and 1013 the present study yields higher values than
490 GEA. We note that primary PM_{10}-imissions may have substantial contributions from wind
491 erosion of agricultural soils (Panagos et al., 2015) that are not incorporated in present
492 anthropogenic inventories. SO_2 exhibits the strongest trend discrepancies with much stronger
493 reductions in trend of the present study as compared to GEA results. As Germany has been
494 reducing SO_2 emissions systematically since the nineteen eighties one would not expect any

495 further strong trends during the time period of the present study. As other studies have
496 demonstrated before, (e.g., van Pinxteren et al., 2019), the maps in Fig. 1 indicate the possibility
497 of imported pollution, in particular from the Southeast. Consequently, we searched for similar
498 trends in emission data reported by EEA for neighboring countries until 2017 directly West,
499 South, and East of Germany, going in the East all the way to Romania. Excel's solver optimized
500 combinations of the EEA-trends for Germany and neighboring countries in order to fit the
501 trends derived in the present study. The solver did not choose German trends for any of the
502 four parameters PM_{10}, BC, SO_2, and NO_x. For PM_{10} a combination of emission trends for the
503 BENELUX countries and France was optimum, albeit without being able to simulate the
504 relative maxima in 2011 and 2013 and the minimum around 2016. For BC the emission trend
505 for the BENELUX countries came closest to the trend of the present study. For SO_2 mostly
506 emissions in Romania with minor contributions from French and BENELUX trends simulated
507 the trends observed over Germany best. NO_x-trends were best simulated by emissions over the
508 Czech and Slovakian countries. Emissions trends over Switzerland, Austria, Hungary and
509 Poland were not utilized by the solver. All simulated trends are displayed as curves EEA in
510 Fig. 6. We do not claim that these simulated trends numerically correspond to imported
511 pollution over Germany. However, the good fit of SO_2-trend with emissions over Romany
512 corroborates our finding of pollution import from Southeastern Europe to Northeastern
513 Germany while the development of BC appears to follow better emission trends over Western
514 neighbor countries than over Germany.
515
516 Sun et al., (2020) investigated trends of size resolved number and eBC mass concentrations
517 at 16 observational sites in Germany from 2009 to 2018 including the three GUAN-sites of the
518 present study. Based on monthly median time series they report average decreases for ME,
519 NG, and WA of -5.5%, -6.1, and -3.9%, respectively. The corresponding result for eBC of the

present study is -4.6%, albeit with a high variability (cf. Fig. 6) of 20 percent units expressed in terms of a standard deviation.

Over the polluted continent the particle-number based parameter $N_{10\text{-}800}$ is largely secondary in nature, i.e., its concentrations are controlled by atmospheric constituents and processes. Thus, there is no primary emission data base with which a similar trend analysis as with PM_{10}, BC, SO_2, and NO_x could be attempted. Instead we chose the 10-year Grand Averages (GA) averages taken over the whole time period of the present study as references from the deviations of annual averages are discussed. Sun et al. (2020) report very minor trends (between -3.5% and 0.1%) for $N_{20\text{-}800}$ at the three GUAN stations of the present study. The 10-year interannual variation of our $N_{10\text{-}800}$ in Fig. 7a) bears out why only a minor trend if any can be expected. For the first four years the annual averages are substantially higher than average. Then annual values decrease down to a minimum in the years 2016/17 before they increase again to a level slightly above the 10-year average.

In Figs 7b-d) annual deviations from the respective GAs are displayed that can be connected to the 10-year course of $N_{10\text{-}800}$. Ozone concentrations averaged over the data from the three GUAN stations can be interpreted as an indicator for photochemical activity that also controls NPF. The annual deviations of O_3 in Fig. 7b) follow rather closely those of $N_{10\text{-}800}$. In Figs 7c) and d) annual deviations of ambient temperature and precipitation rates are displayed that have been averaged over the meteorological data along the back trajectories leading to the four stations. For the temperature an averaging period of 120 trajectory hours yielded the highest (negative) correlation with $N_{10\text{-}800}$ of r = -0.8. After a dip in 2009 annual average trajectory temperatures to a maximum in 2016 before returning to near average in 2018. For the precipitation rates along the trajectories the highest (negative) correlation with $N_{10\text{-}800}$ was found with an averaging period of three days (r=-0.6) before arrival at the stations. The results

546 displayed in Figs 7c) and d) illustrate the complexity of processes and conditions controlling
547 atmospheric particle number concentrations. On one hand, a scavenging effect of precipitation
548 can be used as argument for the high values of $N_{10\text{-}800}$ in the years 2010-2013 and the low values
549 in the years 2014 through 2018. On the other hand, lower annual temperatures during years of
550 relatively high $N_{10\text{-}800}$ and higher than GA-temperatures during years of relatively high $N_{10\text{-}800}$
551 are harder to interpret. Possibly the nucleation of condensable vapors is furthered by lower air
552 temperatures upwind of the stations.
553
554 An important result of trend analysis are the average monthly factors disaggregating the
555 annual emissions. In general the summer minima of the month factors determined in the present
556 study are broader than the curve given by Matthias et al., (2018) for combustion emissions. The
557 decrease of the month factor of PM_{10}, BC, and NO_x in December and the late winter maxima
558 of PM_{10} and SO_2 are not reflected in the Matthias et al., (2018) results. Interestingly, both PM_{10}
559 and SO_2 show a minor secondary peak in June. As an example of the seasonal variability of
560 eBC within an urban source region we averaged the relative annual variation of eBC-
561 concentrations at the station Leipzig Eisenbahnstraße (plotted as curve L-EBS in Fig. 8)
562 exhibiting a smaller seasonal swing than all other curves. The curve for PM_{10} comes closest to
563 that for L-EBS, probably because of agricultural non-combustion emissions in summer.
564
565 In general the downward trends in particulate parameters determined in the present study are
566 similar to temporal trends of particle number and black carbon mass concentrations at 16
567 observational sites in Germany from 2009 to 2018 (Sun et al., 2020). The long-term emission-
568 decrease of PM_{10} as determined in the present study from 2009 to 2018 is smaller than the
569 corresponding number published by the EEA as average over all 28 EU member-states but
570 similar to the figures published by GEA until 2017 (cf. Table 2). For BC, SO_2, and NO_x the
571 present study yields substantially stronger emission-reductions than both GEA and EEA. These

findings are emphasized when considering 2017 as endpoint of the trend calculation (cf. Table 2) at and after which our study shows consistent emission increases of all studied parameters. Comparing the calculated trends with emission trends in neighboring countries as published by the European Environment Agency supports the explanation that the observed trends are to some extent due to changes in imported air masses. Most strongly this holds for SO_2, the trend of which follows that of Romanian emissions rather well.

The last issue we take up in this discussion concerns the frequent residual difference between measured and emission-simulated time series. In Fig. 5, e.g., in most winters there are months when optimized BC-emissions remain substantially lower than the measured monthly medians of eBC. Some information can be gleaned from the "Großwetterlagen", (GWL), representing 29 classifications of large scale weather types after Hess and Brezowsky for Central Europe, (Gerstengarbe and Werner, 1993), provided by the German Weather service for each day (http://www.dwd.de/DE/leistungen/grosswetterlage/grosswetterlage.html). During the winter months with the strongest difference between measured and simulated time series the probabilities of high-pressure systems over Fennoscandia with south-to-southeasterly flow to the four stations is substantially higher than the respective probabilities averaged over the whole ten-year period of the study. This GWL-information is consistent with the back trajectories during the high pollution winter months coming predominantly from the southeasterly sector of the map. While the classified large-scale weather situation with weak dilution of pollution during the winter months is conducive of high particulate concentrations at the receptor sites it does not explain the discrepancy. In principle our simplistic approach of accumulating emissions along back trajectories may be flawed during certain weather situations. However, an alternative explanation could be that the emissions inventories over Eastern and Southeastern Europe in the EDGAR database are somewhat lower than the real emissions.

598

599 6 Summary and conclusions

600

601 Ten years of hourly aerosol and gas data at three stations of the German Ultrafine Aerosol
602 Network GUAN and one station of the Saxonian Environment Agency have been combined
603 with hourly back trajectories to the stations and emission inventories. Measured PM_{10}, particle
604 number concentrations between 10 and 800 nm, and equivalent black carbon were extrapolated
605 along the trajectories. This process yielded what we termed immission maps of these aerosol
606 parameters over Germany. They reflect aerosol emissions modified with atmospheric processes
607 along the air mass transport between sources and the four receptor sites at which potential
608 effects of the particulate air pollution would be realized.

609

610 The ten-year average immission maps do not simply show the distribution of pollution
611 sources upwind of the receptor sites. The comparison with emission data based on the European
612 EDGAR emission database shows that strong Western European emission centers do not
613 dominate the downwind concentrations because their emissions often are reduced by wet
614 scavenging and dilution processes on the way to the receptor area. Maps of average
615 precipitation and wind as they occurred along the trajectories illustrate these processes. In the
616 receptor region mass related aerosol parameters such as PM_{10}, equivalent black carbon, and to
617 some extent also the particle number concentration instead is rather controlled by emissions
618 from Eastern and Southeastern Europe from which pollution transport often occurs under dryer
619 meteorological conditions in continental high-pressure air masses. This finding corresponds to
620 the air mass results derived for the sub-micrometer particle number size distribution by Birmili
621 et al., (2001), by Engler et al., (2007) for the size distribution of non-volatile particles, by Ma
622 et al., (2014) for optical particle properties all evaluated at the station Melpitz, and by van

623 Pinxteren et al., (2019) for transboundary transport of PM_{10} to ten stations in Eastern Germany
624 from neighboring countries. Newly formed particles on the other hand are found in air masses
625 from a broad belt reaching from Burgundy to the Western Czech Republic and Southern Poland,
626 a region with high photochemical activity in summer that is affected by emissions in Northern
627 Italy.
628
629 Annual EDGAR emissions for 2009 of PM_{10}, BC, SO_2, and NO_x, were accumulated along
630 each trajectory and compared the calculated emission sums with the corresponding measured
631 time series on a monthly basis. With a generalized reduced gradient solver the agreement of
632 each pair of monthly time series e.g., measured eBC and BC-emissions was optimized by letting
633 the solver determine both monthly emission factors disaggregating the annual EDGAR
634 emission fields and adjusting the emissions with annual factors modifying the 2009-fields.
635 Relative to 2009 the annual averages of the analyzed air pollutants were lower in 2018 by values
636 between 6% for PM_{10} and 60% for SO_2. In general, the ten-year reductions determined of the
637 present study were stronger than those reported by the German and the European Environmental
638 Agencies. $N_{10\text{-}800}$ exhibited substantial interannual variability but no net decrease over the ten
639 studied years.
640
641 The validity of the present approach of connecting immission and emission of particulate
642 pollution was tested by calculating temporal changes of eBC for subsets of back trajectories
643 passing over two separate prominent emission regions, region A to the Northwest and B to the
644 Southeast of the measuring stations. Consistent with reported emission data the calculated
645 immission decreases over region A are significantly stronger than over region B.
646
647 Compared to published emission monthly factors by Matthias et al., (2018) the present
648 approach yielded broader summer minima that were partly displaced from the midsummer

positions given by Matthias et al., (2018). As an aside we note that during the winter months with extremely high particulate pollution the emissions accumulated along back trajectories often are substantially lower than the measured concentrations which raises the question of the validity of the emission figures in Eastern and Southeastern European source regions.

There are clear limits in the methodology of the present study. Air mass trajectories have inherent uncertainties increasing with their distance travelled (Stohl, 1998). Meteorological processes affecting the aerosol during air mass transport are only considered rather coarsely whereas aerosol dynamics are not considered at all. Possible future improvements concern ensemble trajectories with higher resolution, better meteorological information along the trajectories e.g., radar-derived precipitation as used in Heintzenberg et al., (2018), more comprehensive emission inventories with higher spatiotemporal resolution and higher numbers of analyzed stations.

Acknowledgements

This work was accomplished in the framework of the project ACTRIS-2 (Aerosols, Clouds, and Trace gases Research InfraStructure) under the European Union—Research Infrastructure Action in the frame of the H2020 program for "Integrating and opening existing national and regional research infrastructures of European interest" under Grant Agreement N654109, (H2020—Horizon 2020). Additionally, we acknowledge the WCCAP (World Calibration Centre for Aerosol Physics) as part of the WMO-GAW program base-funded by the German Federal Environmental Agency (UBA). Continuous aerosol measurements as well as data processing at Melpitz, Waldhof and Neuglobsow were supported by the German Federal Environment Agency Grants F&E 370343200 (German title: "Erfassung der Zahl feiner und ultrafeiner Partikel in der Außenluft"), and F&E 371143232 (German title: "Trendanalysen

675 gesundheitsgefährdender Fein-und Ultrafeinstaubfraktionen unter Nutzung der im German
676 Ultrafine Aerosol Network (GUAN) ermittelten Immissionsdaten durch Fortführung und
677 Interpretation der Messreihen). We gratefully acknowledge receiving the emission data set
678 from European emission data base for global atmospheric research (EDGAR). We
679 acknowledge technical support by Annette Pausch of the Saxon State Office for Environment,
680 Agriculture and Geology at the Collmberg station, Achim Grüner und René Rabe (TROPOS)
681 at the Melpitz station, by Olaf Bath (GEA) at the Neuglobsow station, and Andreas Schwerin
682 (GEA) at the Waldhof station. Fabian Senf compiled the "Großwetterlagen" for the present
683 study. We are most grateful for the ideas provided by Peter Winkler in the interpretation of
684 data.
685

686 Literature

687

688 Anderson, J. O., Thundiyil, J. G., and Stolbach, A.: Clearing the air: a review of the effects of
689 particulate matter air pollution on human health, J Med Toxicol, 8, 166-175,
690 10.1007/s13181-011-0203-1, 2012.
691 Beekmann, M., Prévôt, A. S. H., Drewnick, F., Sciare, J., Pandis, S. N., Denier van der Gon,
692 H. A. C., Crippa, M., Freutel, F., Poulain, L., Ghersi, V., Rodriguez, E., Beirle, S.,
693 Zotter, P., von der Weiden-Reinmüller, S. L., Bressi, M., Fountoukis, C., Petetin, H.,
694 Szidat, S., Schneider, J., Rosso, A., El Haddad, I., Megaritis, A., Zhang, Q. J., Michoud,
695 V., Slowik, J. G., Moukhtar, S., Kolmonen, P., Stohl, A., Eckhardt, S., Borbon, A., Gros,
696 V., Marchand, N., Jaffrezo, J. L., Schwarzenboeck, A., Colomb, A., Wiedensohler, A.,
697 Borrmann, S., Lawrence, M., Baklanov, A., and Baltensperger, U.: In situ, satellite
698 measurement and model evidence on the dominant regional contribution to fine
699 particulate matter levels in the Paris megacity, Atmos. Chem. Phys., 15, 9577-9591,
700 10.5194/acp-15-9577-2015, 2015.
701 Birmili, W., Wiedensohler, A., Heintzenberg, J., and Lehmann, K.: Atmospheric particle
702 number size distribution in Central Europe: Statistical relations to air masses and
703 meteorology, J. Geophys. Res., 106, 32005-32018, 2001.
704 Birmili, W., Weinhold, K., Merkel, M., Rasch, F., Sonntag, A., Wiedensohler, A., Bastian, S.,
705 Schladitz, A., Löschau, G., Cyrys, J., Pitz, M., Gu, J., Kusch, T., Flentje, H., Quass, U.,
706 Kaminski, H., Kuhlbusch, T. A. J., Meinhardt, F., Schwerin, A., Bath, O., Ries, L.,
707 Wirtz, K., and Fiebig, M.: Long-term observations of tropospheric particle number size
708 distributions and equivalent black carbon mass concentrations in the German Ultrafine
709 Aerosol Network (GUAN), Earth Syst. Sci. Data, 8, 355-382, doi:10.5194/essd-8-355-
710 2016, 2016.

711 Bond, T. C., Doherty, S. J., Fahey, D. W., Forster, P. M., Berntsen, T., DeAngelo, B. J., Flanner,
712 M. G., Ghan, S., Kärcher, B., Koch, D., Kinne, S., Kondo, Y., Quinn, P. K., Sarofim,
713 M. C., Schultz, M. G., Schulz, M., Venkataraman, C., Zhang, H., Zhang, S., Bellouin,
714 N., Guttikunda, S. K., Hopke, P. K., Jacobson, M. Z., Kaiser, J. W., Klimont, Z.,
715 Lohmann, U., Schwarz, J. P., Shindell, D., Storelvmo, T., Warren, S. G., and Zender,
716 C. S.: Bounding the role of black carbon in the climate system: A scientific assessment,
717 J. Geophys. Res., doi: 10.1002/jgrd.50171, 10.1002/jgrd.50171, 2013.
718 Cass, G. R., and McRae, G. J.: Source-receptor reconciliation of routine air monitoring data for
719 trace metals: An emission inventory assisted approach, Environ. Sci. Technol., 17, 129-
720 139, 1983.
721 Charron, A., Birmili, W., and Harrison, R. M.: Fingerprinting particle origins according to their
722 size distribution at a UK rural site, J. Geophys. Res., 113, D07202,
723 doi:07210.01029/02007JD008562, 2008.
724 Crippa, M., Guizzardi, D., Muntean, M., Schaaf, E., Dentener, F., van Aardenne, J. A., Monni,
725 S., Doering, U., Olivier, J. G. J., Pagliari, V., and Janssens-Maenhout, G.: Gridded
726 emissions of air pollutants for the period 1970–2012 within EDGAR v4.3.2, Earth Syst.
727 Sci. Data, 10, 1987-2013, 10.5194/essd-10-1987-2018, 2018.
728 Diémoz, H., Barnaba, F., Magri, T., Pession, G., Dionisi, D., Pittavino, S., Tombolato, I. K. F.,
729 Campanelli, M., Della Ceca, L. S., Hervo, M., Di Liberto, L., Ferrero, L., and Gobbi, G.
730 P.: Transport of Po Valley aerosol pollution to the northwestern Alps – Part 1:
731 Phenomenology, Atmos. Chem. Phys., 19, 3065-3095, 10.5194/acp-19-3065-2019,
732 2019a.
733 Diémoz, H., Gobbi, G. P., Magri, T., Pession, G., Pittavino, S., Tombolato, I. K. F., Campanelli,
734 M., and Barnaba, F.: Transport of Po Valley aerosol pollution to the northwestern Alps
735 – Part 2: Long-term impact on air quality, Atmos. Chem. Phys., 19, 10129-10160,
736 10.5194/acp-19-10129-2019, 2019b.

737 Draxler, R., and Hess, G.: An overview of the HYSPLIT_4 modeling system for trajectories,
738 dispersion, and deposition, Austr. Meteor. Mag., 47, 295-308, 1998.
739 EEA: Spatial assessment of PM_{10} and ozone concentrations in Europe (2005), European
740 Environmental Agency, Copenhagen, Denmark, 52 pp, 2009.
741 Eliassen, A.: The OECD Study of Long Range Transport of Air Pollutants: Long Range
742 Transport Modelling, Atmos. Environ., 12, 479-487, 1978.
743 Engler, C., Rose, D., Wehner, B., Wiedensohler, A., Brüggemann, E., Gnauk, T., Spindler, G.,
744 Tuch, T., and Birmili, W.: Size distributions of non-volatile particle residuals (Dp<800
745 nm) at a rural site in Germany and relation to air mass origin, Atmos. Chem. Phys., 7,
746 5785-5802, 10.5194/acp-7-5785-2007, 2007.
747 Friedlander, S. K.: Chemical element balances and identification of air pollution sources, Env.
748 Sci. & Technol., 7, 235-240, 10.1021/es60075a005, 1973.
749 Gerstengarbe, F.-W., and Werner, P. C.: Katalog der Grosswetterlagen Europas nach Paul Hess
750 und Helmut Brezowski 1881-1992, 4., vollständ. neu bearb. Aufl., Deutscher
751 Wetterdienst, Offenbach, Germany, 1993.
752 Heintzenberg, J., and Bussemer, M.: Development and application of a spectral light absorption
753 photometer for aerosol and hydrosol samples, J. Aerosol Sci., 31, 801-812, 2000.
754 Heintzenberg, J., Birmili, W., Seifert, P., Panov, A., Chi, X., and Andreae, M. O.: Mapping the
755 aerosol over Eurasia from the Zotino Tall Tower (ZOTTO), Tellus B, 65,
756 doi:http://dx.doi.org/10.3402/tellusb.v3465i3400.20062, 2013.
757 Heintzenberg, J., Leck, C., and Tunved, P.: Potential source regions and processes of aerosol
758 in the summer Arctic, Atmos. Chem. Phys., 15, 6487-6502, 10.5194/acp-15-6487-2015,
759 2015.
760 Heintzenberg, J., Senf, F., Birmili, W., and Wiedensohler, A.: Aerosol connections between
761 distant continental stations, Atmos. Environ., 190, 349-358, 2018.

762 Hůnová, I.: Ambient air quality for the territory of the Czech Republic in 1996–1999 expressed
763 by three essential factors, Sci. Total Environ., 303, 245-251,
764 https://doi.org/10.1016/S0048-9697(02)00493-X, 2003.
765 Hůnová, I., and Bäumelt, V.: Observation-based trends in ambient ozone in the Czech Republic
766 over the past two decades, Atmos. Environ., 172, 157-167,
767 https://doi.org/10.1016/j.atmosenv.2017.10.039, 2018.
768 Kanamitsu, M.: Description of the NMC Global Data Assimilation and Forecast System, Wea.
769 Forecasting, 4, 335-342, 10.1175/1520-0434(1989)004<0335:DOTNGD>2.0.CO;2,
770 1989.
771 Klimont, Z., Kupiainen, K., Heyes, C., Purohit, P., Cofala, J., Rafaj, P., Borken-Kleefeld, J.,
772 and Schöpp, W.: Global anthropogenic emissions of particulate matter including black
773 carbon, Atmos. Chem. Phys., 17, 8681-8723, 10.5194/acp-17-8681-2017, 2017.
774 Krige, D. G.: A statistical approach to some basic mine valuation problems on the
775 Witwatersrand, J. Chem. Metall. Min. Soc. S. Afr., December, 119-159, 1951.
776 Kuenen, J. J. P., Visschedijk, A. J. H., Jozwicka, M., and Denier van der Gon, H. A. C.: TNO-
777 MACC_II emission inventory; a multi-year (2003 - 2009) consistent high-resolution
778 European emission inventory for air quality modelling, Atmos. Chem. Phys., 14, 10963-
779 10976, 10.5194/acp-14-10963-2014, 2014.
780 Kulmala, M., Vehkamäkia, H., Petäjä, T., Dal Maso, M., Lauri, A., Kerminen, V.-M., Birmili,
781 W., and McMurry, P. H.: Formation and growth rates of ultrafine atmospheric particles:
782 a review of observations, J. Aerosol Sci., 35, 143-176, 2004.
783 Lasdon, L. S., Waren, A. D., Jain, A., and Ratner, M.: Design and Testing of a Generalized
784 Reduced Gradient Code for Nonlinear Programming, ACM Trans. Math. Softw., 4, 34–
785 50, 10.1145/355769.355773, 1978.

786 Lavanchy, V. M. H., Gäggeler, H. W., Schotterer, U., Schwikowski, M., and Baltensperger, U.:
787 Historical record of carbonaceous particle concentrations from a European high-alpine
788 glacier (Colle Gnifetti, Switzerland), J. Geophys. Res., 104, 21227-21236, 1999.
789 Leibensperger, E. M., Mickley, L. J., Jacob, D. J., Chen, W. T., Seinfeld, J. H., Nenes, A.,
790 Adams, P. J., Streets, D. G., Kumar, N., and Rind, D.: Climatic effects of 1950 - 2050
791 changes in US anthropogenic aerosols - Part 1: Aerosol trends and radiative forcing,
792 Atmos. Chem. Phys., 12, 3333-3348, 10.5194/acp-12-3333-2012, 2012.
793 Lelieveld, J., Evans, J. S., Fnais, M., Giannadaki, D., and Pozzer, A.: The contribution of
794 outdoor air pollution sources to premature mortality on a global scale, Nature, 525, 367-
795 371, 10.1038/nature15371, 2015.
796 Li, Z., Niu, F., Fan, J., Liu, Y., Rosenfeld, D., and Ding, Y.: Long-term impacts of aerosols on
797 the vertical development of clouds and precipitation, Nature Geosci., 4, 888-894, 2011.
798 Liu, S., Hua, S., Wang, K., Qiu, P., Liu, H., Wu, B., Shao, P., Liu, X., Wu, Y., Xue, Y., Hao,
799 Y., and Tian, H.: Spatial-temporal variation characteristics of air pollution in Henan of
800 China: Localized emission inventory, WRF/Chem simulations and potential source
801 contribution analysis, Sci. Total Environ., 624, 396-406,
802 https://doi.org/10.1016/j.scitotenv.2017.12.102, 2018.
803 Lugauer, M., and Winkler, P.: Thermal circulation in South Bavaria – climatology and synoptic
804 aspects, Meteor. Z., 14, 15-30, 2005.
805 Ma, N., Birmili, W., Müller, T., Tuch, T., Cheng, Y. F., Xu, W. Y., Zhao, C. S., and
806 Wiedensohler, A.: Tropospheric aerosol scattering and absorption over central Europe:
807 a closure study for the dry particle state, Atmos. Chem. Phys., 14, 6241-6259,
808 10.5194/acp-14-6241-2014, 2014.
809 Marmer, E., and Langmann, B.: Aerosol modeling over Europe: 1. Interannual variability of
810 aerosol distribution, J. Geophys. Res., 112, D23S15, doi:10.1029/2006JD008113, 2007.

Matthias, V., Arndt, J. A., Aulinger, A., Bieser, J., Denier van der Gon, H., Kranenburg, R., Kuenen, J., Neumann, D., Pouliot, G., and Quante, M.: Modeling emissions for three-dimensional atmospheric chemistry transport models, Journal of the Air & Waste Management Association, 68, 763-800, 10.1080/10962247.2018.1424057, 2018.

Miller, M. S., Friedlander, S. K., and Hidy, G. M.: A chemical element balance for the Pasadena aerosol, J. Colloid Interface Sci., 39, 165-176, https://doi.org/10.1016/0021-9797(72)90152-X, 1972.

Minkos, A., Dauert, U., Feigenspan, S., and Kessinger, S.: . German Environment Agency, Jan 2019, D-06813 , 28 pp. , Accessed on September 6, 2019 [Online] Available: https://www.umweltbundesamt.de/sites/default/files/medien/1410/publikationen/190329_uba_hg_luftqualitaet_engl_bf.pdf: Air Quality 2018 - Preliminary Evaluation, German Environment Agency, Dessau-Rosslau, Germany, 28, 2019.

Monks, P. S., Archibald, A. T., Colette, A., Cooper, O., Coyle, M., Derwent, R., Fowler, D., Granier, C., Law, K. S., Mills, G. E., Stevenson, D. S., Tarasova, O., Thouret, V., von Schneidemesser, E., Sommariva, R., Wild, O., and Williams, M. L.: Tropospheric ozone and its precursors from the urban to the global scale from air quality to short-lived climate forcer, Atmos. Chem. Phys., 15, 8889-8973, 10.5194/acp-15-8889-2015, 2015.

Müller, T., Henzing, J. S., de Leeuw, G., Wiedensohler, A., Alastuey, A., Angelov, H., Bizjak, M., Collaud Coen, M., Engström, J. E., Gruening, C., Hillamo, R., Hoffer, A., Imre, K., Ivanow, P., Jennings, G., Sun, J. Y., Kalivitis, N., Karlsson, H., Komppula, M., Laj, P., Li, S. M., Lunder, C., Marinoni, A., Martins dos Santos, S., Moerman, M., Nowak, A., Ogren, J. A., Petzold, A., Pichon, J. M., Rodriquez, S., Sharma, S., Sheridan, P. J., Teinilä, K., Tuch, T., Viana, M., Virkkula, A., Weingartner, E., Wilhelm, R., and Wang, Y. Q.: Characterization and intercomparison of aerosol absorption photometers: result of two intercomparison workshops, Atmos. Meas. Tech., 4, 245-268, 10.5194/amt-4-245-2011, 2011.

837 Nordmann, S., Birmili, W., Weinhold, K., Müller, K., Spindler, G., and Wiedensohler, A.:
838 Measurements of the mass absorption cross section of atmospheric soot particles using
839 Raman spectroscopy, J. Geophys. Res., 118, 12,075-012,085, 10.1002/2013JD020021,
840 2013.
841 Panagos, P., Borrelli, P., Poesen, J., Ballabio, C., Lugato, E., Meusburger, K., Montanarella,
842 L., and Alewell, C.: The new assessment of soil loss by water erosion in Europe,
843 Environmental Science & Policy, 54, 438-447, 10.1016/j.envsci.2015.08.012, 2015.
844 Patashnick, H., and Rupprecht, E. G.: Continuous PM-10 Measurements Using the Tapered
845 Element Oscillating Microbalance, Journal of the Air & Waste Management
846 Association, 41, 1079-1083, 10.1080/10473289.1991.10466903, 1991.
847 Penner, J. E., Dong, X., and Chen, Y.: Observational evidence of a change in radiative forcing
848 due to the indirect aerosol effect, Nature, 427, 231-234, 2004.
849 Petzold, A., Ogren, J. A., Fiebig, M., Laj, P., Li, S. M., Baltensperger, U., Holzer-Popp, T.,
850 Kinne, S., Pappalardo, G., Sugimoto, N., Wehrli, C., Wiedensohler, A., and Zhang, X.
851 Y.: Recommendations for reporting "black carbon" measurements, Atmos. Chem.
852 Phys., 13, 8365-8379, 10.5194/acp-13-8365-2013, 2013.
853 Pruppacher, H. R., and Klett, J. D.: Microphysics of Clouds and Precipitation, Reidel Publishing
854 Co., Dordrecht, 714pp, 1978.
855 Rehme, R.: Application of Gas Phase Titration in the Calibration of Nitric Oxide, Nitrogen
856 Dioxide, and Ozone Analyzers, in: Calibration in Air Monitoring, edited by: Chapman,
857 R., and Sheesley, D., ASTM International, West Conshohocken, PA, 198-209, 1976.
858 Reitebuch, O., Dabas, A., Delville, P., Drobinsk, P., and Gantner, L.: Characterization of Alpine
859 pumping by airborne Doppler lidar and numerical simulations., Int. Conf. Alp. Meteor.,
860 Brig 2003. – Publications of MeteoSwiss, 66, 134-137, 2003.
861 Riemer, N., Vogel, H., and Vogel, B.: Soot aging time scales in polluted regions during day
862 and night, Atmos. Chem. Phys., 4, 1885-1893, 2004.

Rohde, R. A., and Muller, R. A.: Air Pollution in China: Mapping of Concentrations and Sources, PLoS One, 10, e0135749-e0135749, 10.1371/journal.pone.0135749, 2015.

Samset, B. H., Sand, M., Smith, C. J., Bauer, S. E., Forster, P. M., Fuglestvedt, J. S., Osprey, S., and Schleussner, C. F.: Climate Impacts From a Removal of Anthropogenic Aerosol Emissions, Geophysical Research Letters, 45, 1020-1029, 10.1002/2017gl076079, 2018.

Schell, B., Ackermann, I., Hass, H., Binkowski, F., and Ebel, A.: Modeling the formation of secondary organic aerosol within a comprehensive air quality model system, J. Geophys. Res., 106, 28275–28293, 2001.

Schwartz, S. E.: The whitehouse effect - shortwave radiative forcing of climate by anthropogenic aerosols: an overview, J. Aerosol Sci., 27, 359-382, 1996.

Sen, P. K.: Estimates of the Regression Coefficient Based on Kendall's Tau, J. Am. Stat. Assoc., 63, 1379–1389, 1968.

Spindler, G., Müller, K., and Herrmann, H.: Main particulate matter components in Saxony (Germany) - trends and sampling aspects, Environ. Sci. Pollut. Res., 6, 89-94, 1999.

Spindler, G., Grüner, A., Müller, K., Schlimper, S., and Herrmann, H.: Long-term size-segregated particle (PM10, PM2.5, PM1) characterization study at Melpitz -- influence of air mass inflow, weather conditions and season, J. Atmos. Chem., 70, 165-195, 10.1007/s10874-013-9263-8, 2013.

Stein, A. F., Draxler, R. R., Rolph, G. D., Stunder, B. J. B., Cohen, M. D., and Ngan, F.: NOAA's HYSPLIT Atmospheric Transport and Dispersion Modeling System, Bull. Amer. Meteor. Soc., 96, 2059-2077, 10.1175/BAMS-D-14-00110.1, 2015.

Stohl, A.: Trajectory statistics - a new method to establish source-receptor relationships of air pollutants and its application to the transport of particulate sulfate in Europe, Atmos. Environ., 30, 579-587, 1996.

888 Stohl, A.: Computations, accuracy and applications of trajectories - A review and bibliography,
889 Atmos. Environ., 32, 947-966, 1998.
890 Struzewska, J., and Jefimow, M.: A 15-year analysis of surface ozone pollution in the context
891 of hot spells episodes over Poland, Acta Geophysica, 64, 1875-1902, 10.1515/acgeo-
892 2016-0067, 2013.
893 Sun, J., Birmili, W., Hermann, M., Tuch, T., Weinhold, K., Spindler, G., Schladitz, A., Bastian,
894 S., Löschau, G., Cyrys, J., Gu, J., Flentje, H., Briel, B., Asbach, C., Kaminski, H., Ries,
895 L., Sohmer, R., Gerwig, H., Wirtz, K., Meinhardt, F., Schwerin, A., Bath, O., Ma, N.,
896 and Wiedensohler, A.: Variability of Black Carbon Mass Concentrations, Sub-
897 micrometer Particle Number Concentrations and Size Distributions: Results of the
898 German Ultrafine Aerosol Network Ranging from City Street to High Alpine Locations,
899 Atmos. Environ., 202, 256-268, https://doi.org/10.1016/j.atmosenv.2018.12.029, 2019.
900 Sun, J., Birmili, W., Hermann, M., Tuch, T., Weinhold, K., Merkel, M., Rasch, F., Müller, T.,
901 Schladitz, A., Bastian, S., Löschau, G., Cyrys, J., Gu, J., Flentje, H., Briel, B., Asbach,
902 C., Kaminski, H., Ries, L., Sohmer, R., Gerwig, H., Wirtz, K., Meinhardt, F., Schwerin,
903 A., Bath, O., Ma, N., and Wiedensohler, A.: Decreasing Trends of Particle Number and
904 Black Carbon Mass Concentrations at 16 Observational Sites in Germany from 2009 to
905 2018, Atmos. Chem. Phys., 2019, 1-19, 10.5194/acp-2019-754, 2020.
906 Swietlicki, E., Svantesson, B., and Hansson, H.-C.: European source area apportionment, J.
907 Aerosol Sci., 19, 1175-1178, 1988.
908 Theil, H.: A Rank-Invariant Method of Linear and Polynomial Regression Analysis, in: Henri
909 Theil's Contributions to Economics and Econometrics: Econometric Theory and
910 Methodology, edited by: Raj, B., and Koerts, J., Springer Netherlands, Dordrecht, 345–
911 381, 1992.
912 Twomey, S.: Pollution and the planetary albedo, Atmos. Environ., 8, 1251-1256, 1974.

van Pinxteren, D., Mothes, F., Spindler, G., Fomba, K. W., and Herrmann, H.: Trans-boundary PM10: Quantifying impact and sources during winter 2016/17 in eastern Germany, Atmos. Environ., 200, 119-130, https://doi.org/10.1016/j.atmosenv.2018.11.061, 2019.

Wehner, B., Siebert, H., Stratmann, F., Tuch, T., Wiedensohler, A., Petäjä, T., Dal Maso, M., and Kulmala, M.: Horizontal homogeneity and vertical extent of new particle formation events, Tellus, 59 B, 362-371, 2007.

Wichmann, H. E., and Peters, A.: Epidemiological evidence of the effects of ultrafine particle exposure, Philosophical Transactions of the Royal Society of London, 358, 1751-2769, 2000.

Wiedensohler, A., Birmili, W., Nowak, A., Sonntag, A., Weinhold, K., Merkel, M., Wehner, B., Tuch, T., Pfeifer, S., Fiebig, M., Fjäraa, A. M., Asmi, E., Sellegri, K., Depuy, R., Venzac, H., Villani, P., Laj, P., Aalto, P., Ogren, J. A., Swietlicki, E., Williams, P., Roldin, P., Quincey, P., Hüglin, C., Fierz-Schmidhauser, R., Gysel, M., Weingartner, E., Riccobono, F., Santos, S., Grüning, C., Faloon, K., Beddows, D., Harrison, R., Monahan, C., Jennings, S. G., O'Dowd, C. D., Marinoni, A., Horn, H. G., Keck, L., Jiang, J., Scheckman, J., McMurry, P. H., Deng, Z., Zhao, C. S., Moerman, M., Henzing, B., de Leeuw, G., Löschau, G., and Bastian, S.: Mobility particle size spectrometers: harmonization of technical standards and data structure to facilitate high quality long-term observations of atmospheric particle number size distributions, Atmos. Meas. Tech., 5, 657-685, 10.5194/amt-5-657-2012, 2012.

Wiedensohler, A., Wiesner, A., Weinhold, K., Birmili, W., Hermann, M., Merkel, M., Müller, T., Pfeifer, S., Schmidt, A., Tuch, T., Velarde, F., Quincey, P., Seeger, S., and Nowak, A.: Mobility particle size spectrometers: Calibration procedures and measurement uncertainties, Aerosol Sci. Technol., 52, 146-164, 10.1080/02786826.2017.1387229, 2018.

Winkler, P., Lugauer, M., and Reitebuch, O.: Alpine Pumping, PROMET, 32, 34-42, 2006.

939 Wolke, R., Hellmuth, O., Knoth, O., Schröder, W., Heinrich, B., and Renner, E.: The chemistry-
940 transport modeling system LM-MUSCAT: Description and CityDelta applications, in:
941 Air Pollution Modeling and its Application XVI, Kluwer Academic/Plenum, 427–439,
942 2004.
943 Zanatta, M., Gysel, M., Bukowiecki, N., Müller, T., Weingartner, E., Areskoug, H., Fiebig, M.,
944 Yttri, K. E., Mihalopoulos, N., Kouvarakis, G., Beddows, D., Harrison, R. M., Cavalli,
945 F., Putaud, J. P., Spindler, G., Wiedensohler, A., Alastuey, A., Pandolfi, M., Sellegri,
946 K., Swietlicki, E., Jaffrezo, J. L., Baltensperger, U., and Laj, P.: A European aerosol
947 phenomenology-5: Climatology of black carbon optical properties at 9 regional
948 background sites across Europe, Atmos. Environ., 145, 346-364,
949 10.1016/j.atmosenv.2016.09.035, 2016.
950 Zhu, K., Zhang, J., and Lioy, P. J.: Evaluation and Comparison of Continuous Fine Particulate
951 Matter Monitors for Measurement of Ambient Aerosols, Journal of the Air & Waste
952 Management Association, 57, 1499-1506, 10.3155/1047-3289.57.12.1499, 2007.
953

954 Table 1: Characteristics of the four stations of the present study, see text for instrumental details. The number of validated data hours are
955 given for each component

Station	Acronym	Latitude	Longitude	MPSS[1]	eBC[2]	PM10 continous[3,4]	PM10 discontinous[5]	NO_x[6]	SO_2[7]	O_3[8]
Collmberg	CO	51.3	13			85054		88838		88792
Melpitz	ME	51.5	12.9	81561	88196		88822	86260	85541	84421
Neuglobsow	NG	53.1	13	57962	77540	71202		83718	87778	87943
Waldhof	WA	52.8	10.8	84276	80725	88321		85503	82386	87373

[1]MPSS - scanning mobility particle size spectrometer TROPOS (10 – 800 nm); [2]MAAP - Multi-angle absorption photometer 5012 Thermo Fischer Scientific; [3]TEOM-FDM - Tapered element oscillating microbalance fitted with a filter dynamics measuring system 1405 Thermo Fischer Scientific; [4]SCHARP - Synchronized Hybrid Ambient Real-time Particulate Monitor 5030 Thermo Fischer Scientific; [5]HVS – High Volume Sampler DIGITEL DH-80; [6]TLA-NOx –Trace Level NOx Analyzer 42i-TL Thermo Fischer Scientific; [7]TLA-SO2 - Trace Level SO_2 Analyzer 43i-TLE Thermo Fischer Scientific; [8]

956

957

Table 2 Median concentrations of eBC concentrations (μgm^{-3}) and temporal trends (2009-2018) of eBC in terms of Sen-Theil slope (% per year) as determined for air masses passing over Regions A and B as analyzed at the stations Melpitz (ME), Neuglobsow (NG), and Waldhof (WA). For comparison the national annual decreases in BC emissions 2009-2017 in % according to the European Environmental Agency are added.

	DELTA T*	No. of back trajectories			Median eBC in µm/m³			Sen-Theil slope in % per year				Decrease in national BC emissions in % per year		
	in h	**ME**	**NG**	**WA**	**ME**	**NG**	**WA**	**ME**	**NG**	**WA**	**3 Stations****	Belgium	Netherlands	Germany
	1	21941	17514	27218	0.38	0.40	0.41	-6.40	-6.80	-4.80	-5.85	-6.1%	-6.1%	-4.9%
Region A	3	18605	14268	22132	0.38	0.40	0.41	-6.40	-6.90	-4.80	-5.89			
B-NL-NRW	6	14802	10086	15936	0.39	0.40	0.42	-6.40	-7.60	-5.10	-6.19			
	12	6817	3746	6131	0.40	0.50	0.50	-7.10	-7.90	-5.30	-6.62			
												Czech Rep.	Poland	Slovakia
	1	11096	5264	4191	1.10	1.19	1.13	-3.60	-3.40	-1.70	-3.16	-2.8%	0.5%	-2.3%
Region B	3	9601	4339	3541	1.08	1.18	1.12	-3.40	-3.40	-2.10	-3.14			
CZ-PL-SK	6	7000	3062	2570	1.05	1.09	1.11	-4.00	-2.90	-2.70	-3.47			
	12	3628	1410	1277	1.00	1.00	1.00	-3.70	-3.00	-2.70	-3.34			
ALL		85846	75190	78356	0.45	0.36	0.36	-5.90	-5.60	-4.00	-5.18			
Sun (2020)								-4.40	-7.80	-3.20				

* Minimum time spent over the specified source region, **Weighted mean, according to the available number of back trajectories

962 Table 3 Percental decreases in the anthropogenic emissions of PM_{10}, BC, SO_2, and
963 NO_x relative to 2009 as reported by the European Environment Agency (EEA,
964 https://www.eea.europa.eu/data-and-maps/dashboards/air-pollutant-emissions-data-
965 viewer-2), the German Environment Agency (GEA), and calculated in the present
966 study. The EEA and GEA only report data until 2017, (*=BC until 2016).

967

Component	EEA 2009-2017	GEA 2009-2017	GUAN emissions 2009-2017	GUAN emissions 2009-2018
PM_{10}	12%	4.2%	16%	6%
BC*	29%	35%*	63%	44%
SO_2	33%	20%	68%	59%
NO_x	20%	11%	43%	30%

968

969

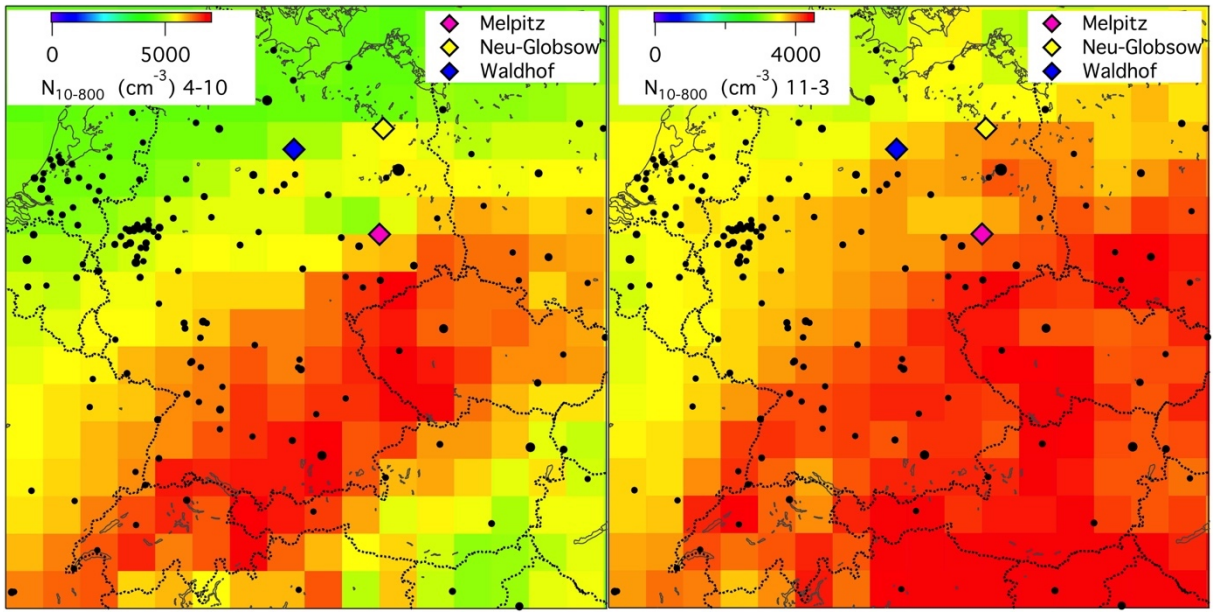

Fig. 1 Maps of particle number concentration $N_{10\text{-}800}$ (cm^{-3}) extrapolated under 1000 m height along five day back trajectories from hourly data at the four stations from 2009 to 2018; left: months April through October; right: months November through March. The GUAN-stations are marked with colored diamonds. The Collmberg station lies 30 km Southeast of station Melpitz. Here and in the following maps the black dots represent cities larger than 100000 inhabitants with the size of the dots being proportional to the number of inhabitants.

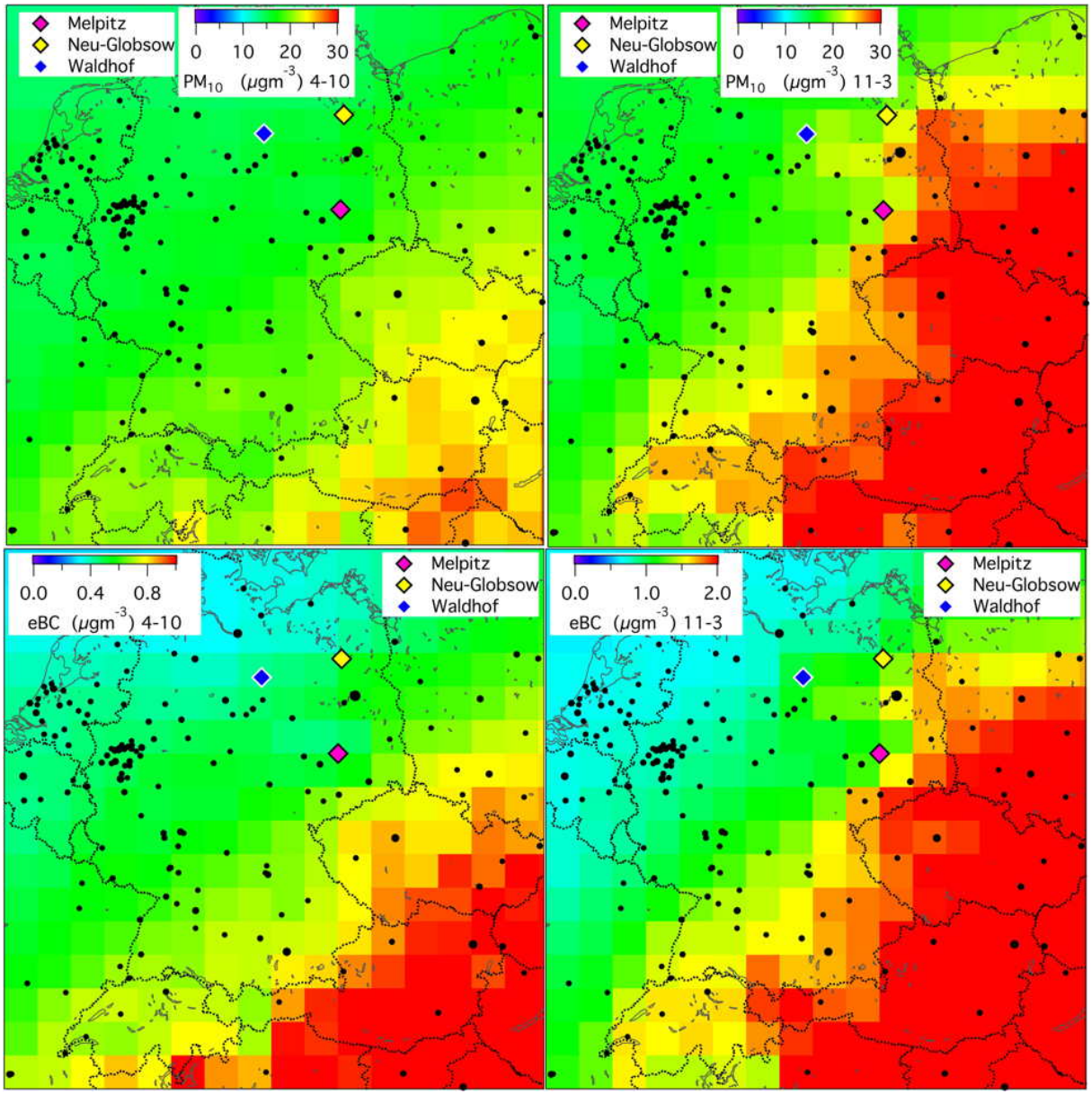

979

980 Fig. 2 As Fig. 1 but for particle mass concentrations (top, PM_{10}, μgcm^{-3}), and black carbon

981 concentrations (bottom, eBC, μgm^{-3}).

982

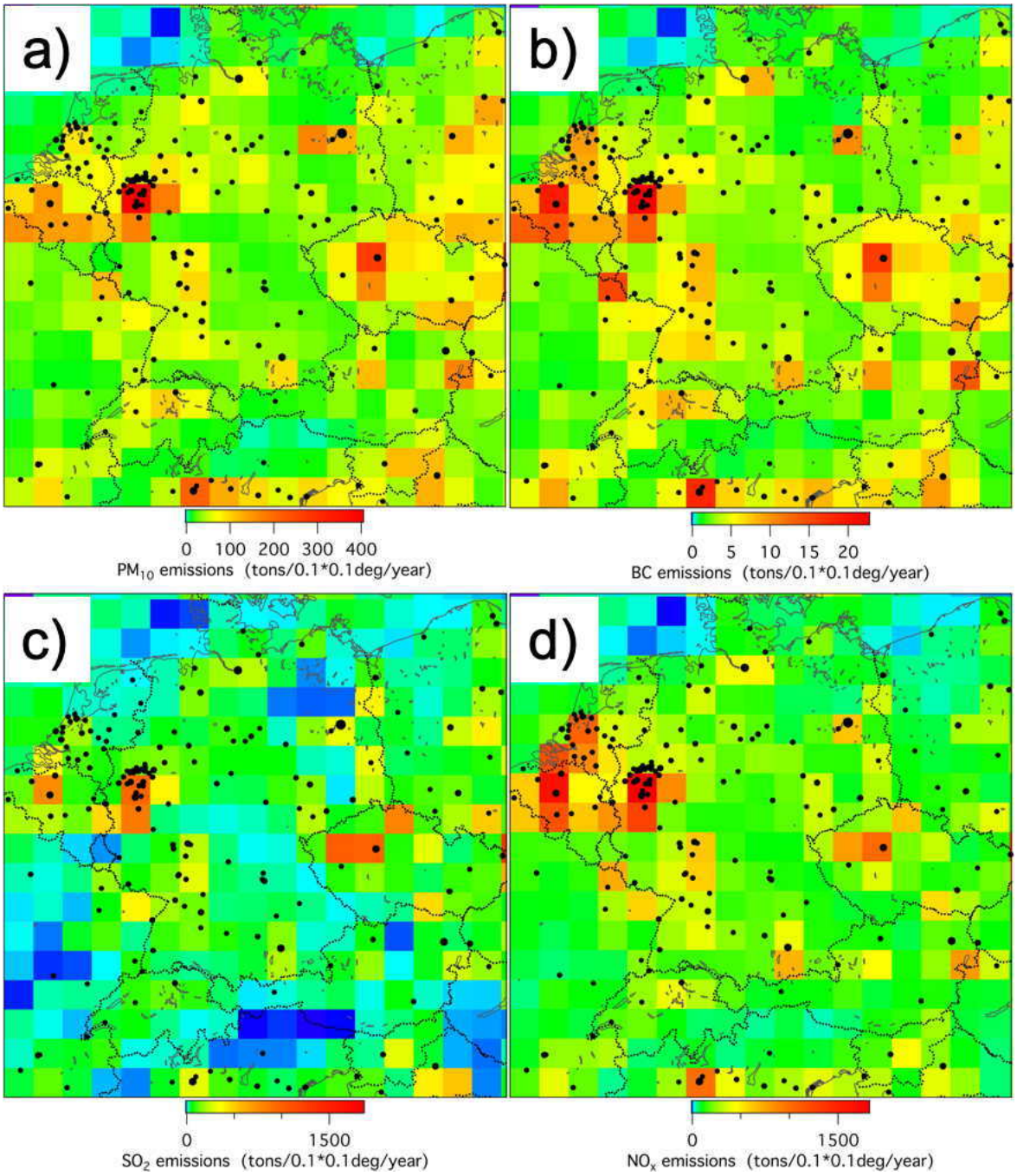

983

984 Fig. 3 As Fig. 1 but a) for PM_{10} emissions (tons/0.1*0.1deg./year), b) for BC emissions, c) for
985 SO_2 emissions, and d) for NO_x emissions (tons/0.1*0.1deg./year) according to the
986 EDGAR emission database
987 (https://data.europa.eu/doi/10.2904/JRC_DATASET_EDGAR) for 2009 averaged over
988 the geogrid of the present study.

989

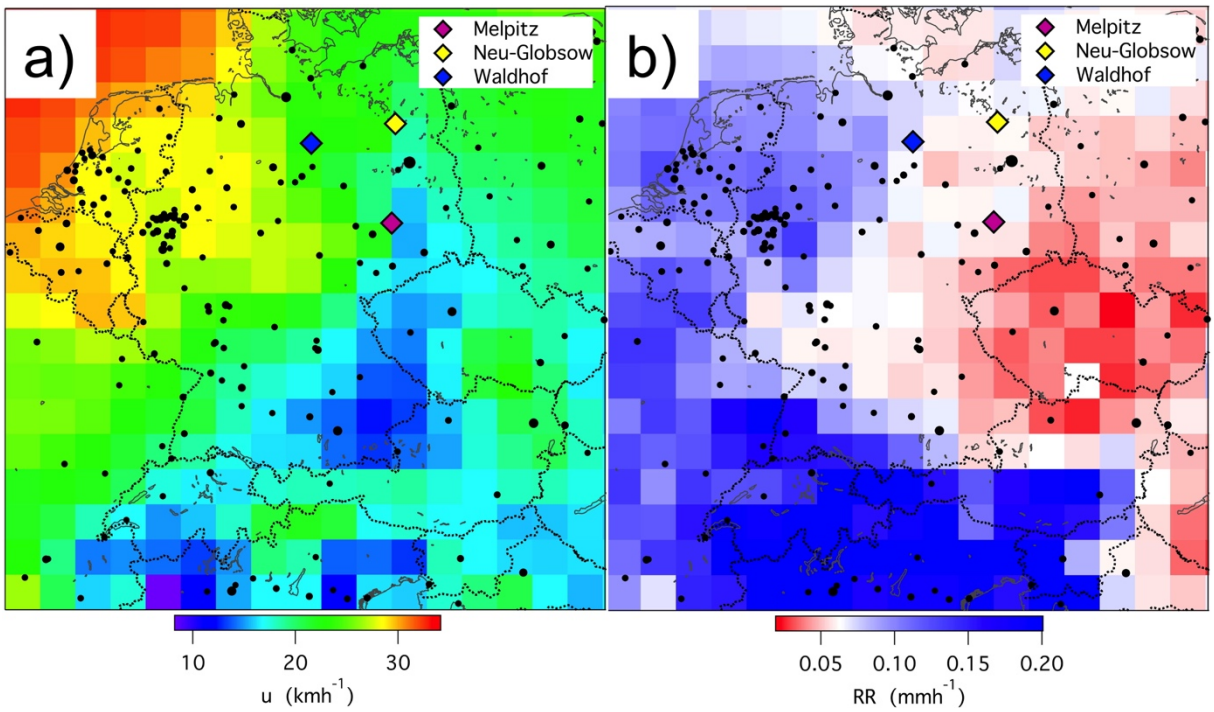

990

991 Fig. 4 a) Map of horizontal wind speed (u, kmh^{-1}) as reported by HYSPLIT along hourly five-
992 day back trajectories to the four stations marked in the graph averaged over the time
993 period 2009 to 2018; b) as a) but for precipitation (RR, mmh^{-1}).

994

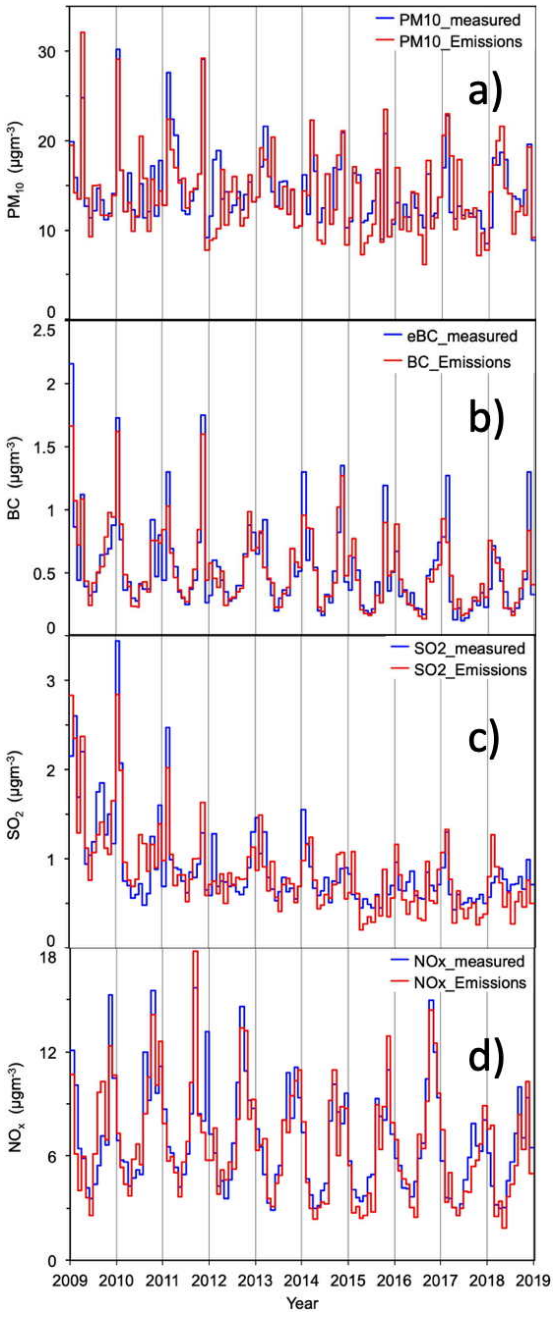

995

996 Fig. 5 a) Monthly medians of PM_{10}-concentrations at the four stations of the present study
997 (blue), and monthly medians of optimized sums of PM_{10}-emissions along back
998 trajectories leading to the stations (red). b) as a) but for measured eBC-concentrations
999 and BC-emissions along back trajectories. c) as a) but for measured SO_2-concentrations
1000 and SO_2-emissions along back trajectories. d) as a) but for measured NO_x-
1001 concentrations and NO_x -emissions along back trajectories.

1002

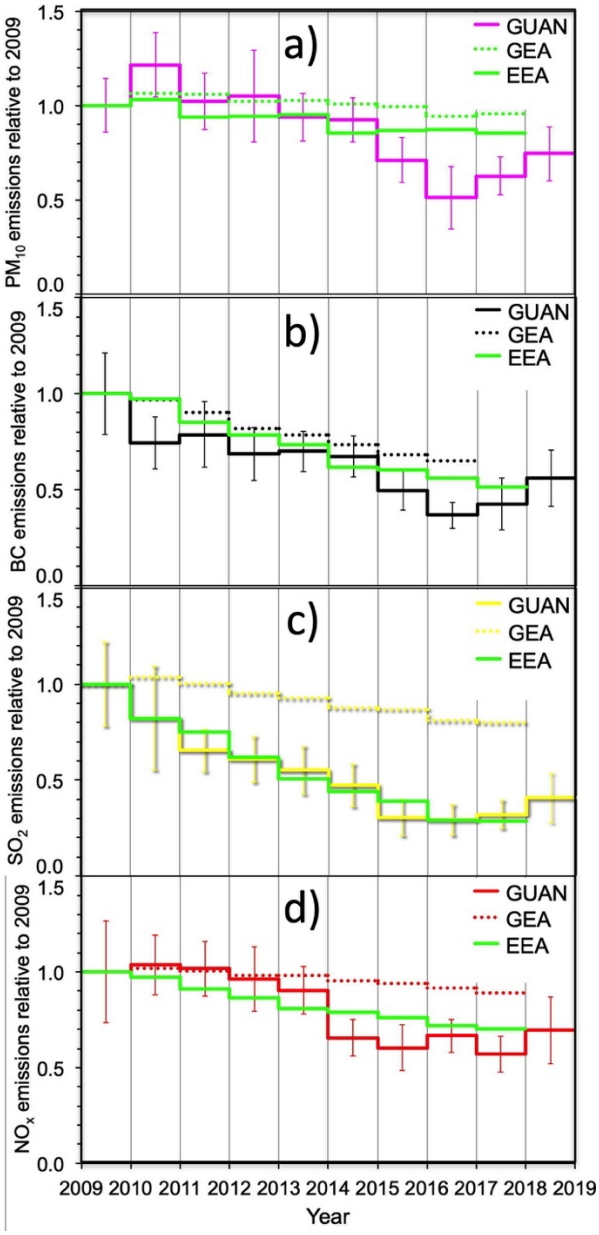

1003

1004 Fig. 6 GUAN: Trends in the emissions of a) PM_{10}, b) BC, c) SO_2, and d) NO_x, relative to 2009
1005 as calculated by optimizing the agreement between 2009-EDGAR-emissions and
1006 concentrations measured at the four stations of the present study. The error bars
1007 represent annual average relative deviations between measured and simulated data.
1008 GEA: Trends as reported for Germany by the German Environment Agency. EEA:
1009 Trends as optimized from combinations of trends over Germany and neighboring
1010 countries, (see text for details).

1011

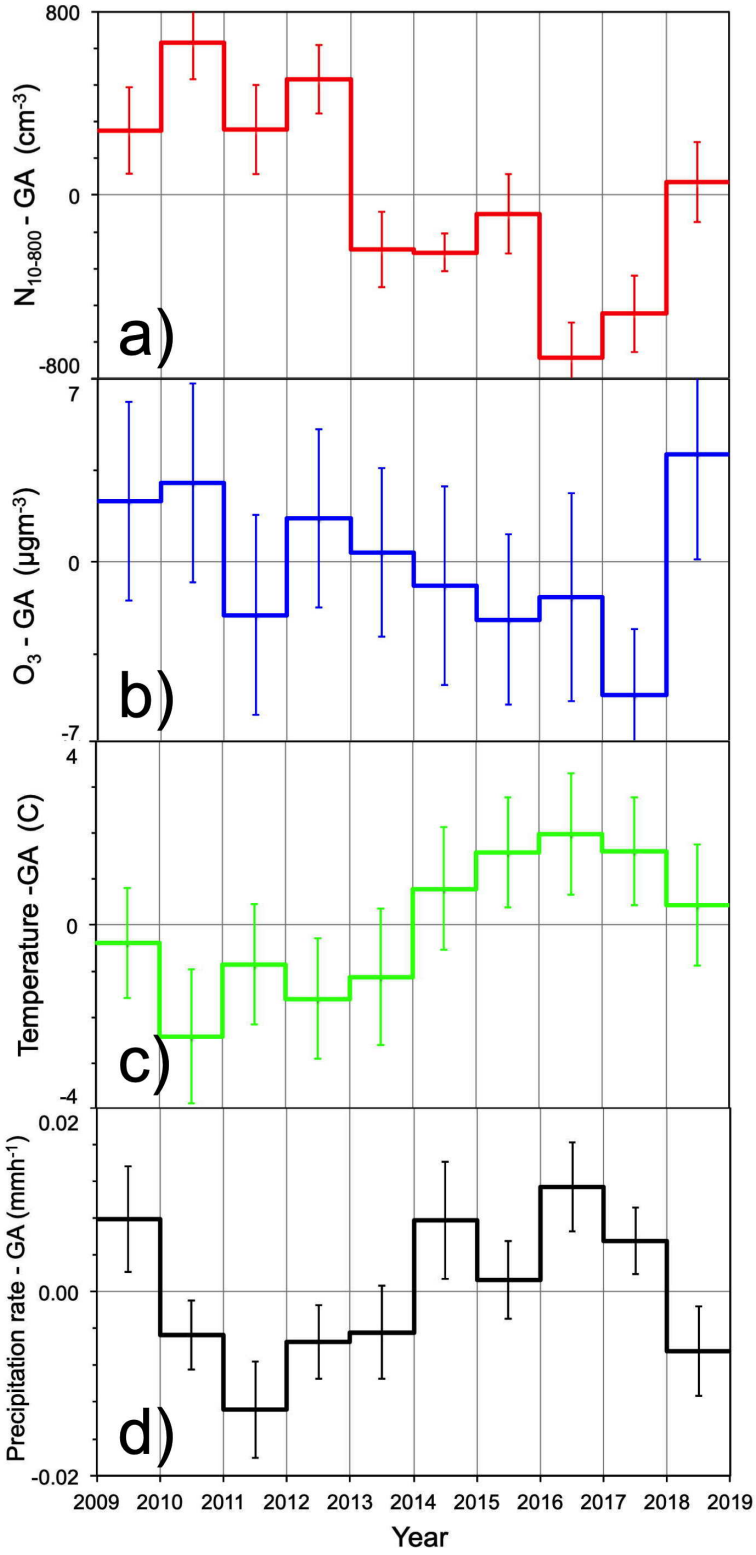

1012

1013 Fig. 7 Trends in annual average deviations a) $\Delta N_{10\text{-}800}$, b) ΔO_3, c) temperature ΔT along the

1014 trajectories five days back in time, and d) precipitation rate ΔRR along the trajectories

1015 three days back in time. The deviations are taken relative to the respective 10-year

1016 Grand Average (GA). The error bars represent the standard deviations of the annual
1017 averages.
1018

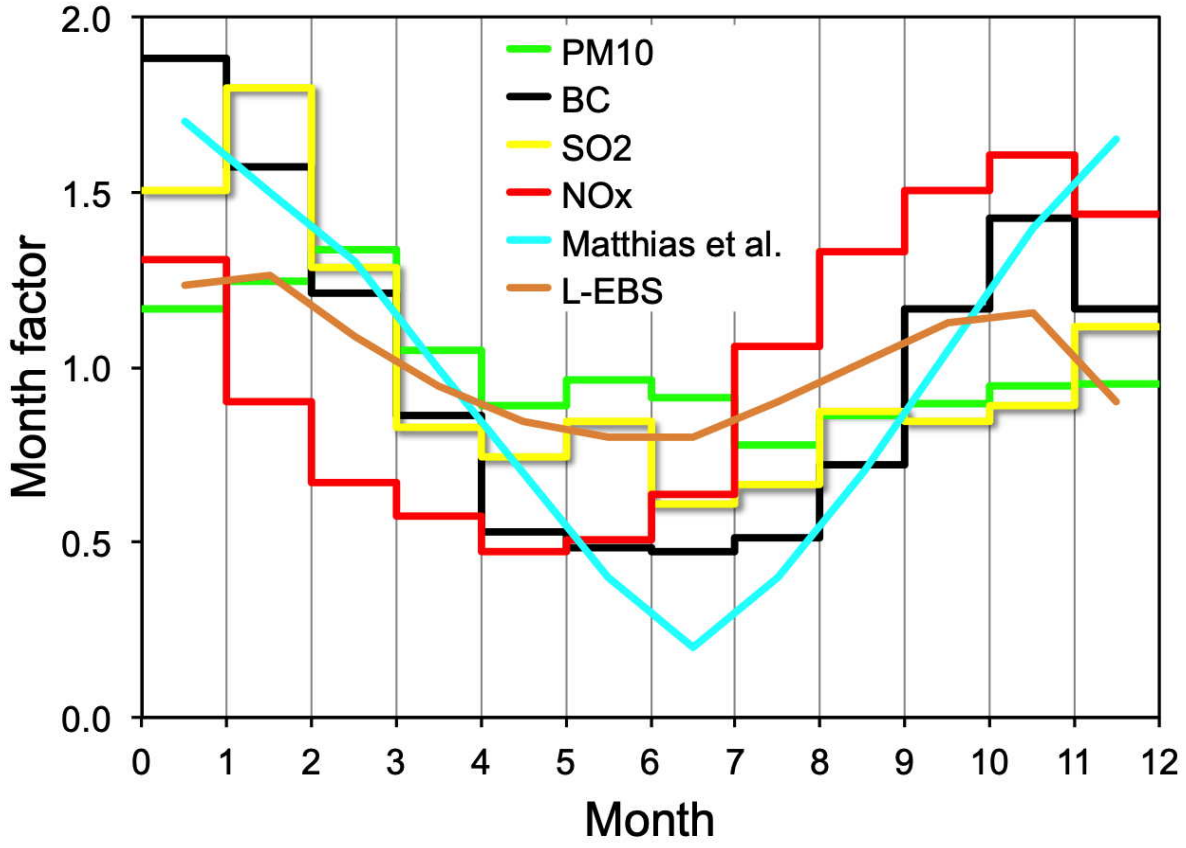

Fig. 8 Month factors for the emissions of PM_{10}, BC, SO_2, and NO_x as determined by optimizing the agreement between EDGAR-emissions and concentrations measured at the four stations of the present study. For comparison the month factors of Matthias et al., (2018) for combustion emissions are plotted and the relative annual variation of eBC concentrations measured at the station Leipzig-Eisenbahnstraße (L-EBS) averaged over the time period of the present study.